Research article



Regulatory dynamics of the higher-plant PSI-LHCI supercomplex during state transitions

Jianghao Wu^{1,6}, Shuaijiabin Chen^{2,3,6}, Chao Wang¹, Weijun Lin^{1,5}, Chao Huang¹, Chengxu Fan¹, Dexian Han¹, Dandan Lu¹, Xiumei Xu¹, SenFang Sui^{2,3,4,*} and Lixin Zhang^{1,*}

1State Key Laboratory of Crop Stress Adaptation and Improvement, School of Life Sciences, Henan University, Jinming Avenue, Kaifeng 475004, China

https://doi.org/10.1016/j.molp.2023.11.002

ABSTRACT

State transition is a fundamental light acclimation mechanism of photosynthetic organisms in response to the environmental light conditions. This process rebalances the excitation energy between photosystem I (PSI) and photosystem II through regulated reversible binding of the light-harvesting complex II (LHCII) to PSI. However, the structural reorganization of PSI-LHCI, the dynamic binding of LHCII, and the regulatory mechanisms underlying state transitions are less understood in higher plants. In this study, using cryoelectron microscopy we resolved the structures of PSI-LHCI in both state 1 (PSI-LHCI-ST1) and state 2 (PSI-LHCI-ST2) from *Arabidopsis thaliana*. Combined genetic and functional analyses revealed novel contacts between Lhcb1 and PsaK that further enhanced the binding of the LHCII trimer to the PSI core with the known interactions between phosphorylated Lhcb2 and the PsaL/PsaH/PsaO subunits. Specifically, PsaO was absent in the PSI-LHCI-ST1 supercomplex but present in the PSI-LHCI-LHCII-ST2 supercomplex, in which the PsaL/PsaK/PsaA subunits undergo several conformational changes to strengthen the binding of PsaO in ST2. Furthermore, the PSI-LHCI module adopts a more compact configuration with shorter Mg-to-Mg distances between the chlorophylls, which may enhance the energy transfer efficiency from the peripheral antenna to the PSI core in ST2. Collectively, our work provides novel structural and functional insights into the mechanisms of light acclimation during state transitions in higher plants.

Key words: state transitions, dynamic conformation, photosystem I, regulatory mechanism, Arabidopsis thaliana

Wu J., Chen S., Wang C., Lin W., Huang C., Fan C., Han D., Lu D., Xu X., Sui S., and Zhang L. (2023). Regulatory dynamics of the higher-plant PSI-LHCI supercomplex during state transitions. Mol. Plant. 16, 1937–1950.

INTRODUCTION

During oxygenic photosynthesis in higher plants, algae, and cyanobacteria, solar energy is absorbed by peripheral light-harvesting complexes (LHCs) and transferred to the reaction centers of photosystems I and II (PSI and PSII, respectively), where charge separation occurs, giving rise to electron flow along the photosynthetic electron transport chain (Rochaix, 2014; Govindjee and Bjorn, 2017; Croce and Van Amerongen, 2020). In higher plants, LHCI, encoded by Lhca1–Lhca4, is attached to the PSI core in monomeric form, forming the PSI–LHCI complex, while LHCII, encoded by Lhcb1–Lhcb6, is mostly associated with the PSII core to constitute the PSII–LHCII complex (Nelson and Yocum, 2006; Pan et al., 2020). More specifically, Lhcb4–Lhcb6 are organized in

monomeric form, whereas Lhcb1–Lhcb3 are assembled as homoor heterotrimers to form the major antenna of PSII (Caffarri et al., 2009; Su et al., 2017; Van Bezouwen et al., 2017). Due to the difference in light absorption preference between PSI and PSII, changes in light conditions could result in unbalanced excitation of these two PSs, leading to a decreased photosynthetic yield in the absence of state transitions (Eberhard et al., 2008; Rochaix, 2013).

To redistribute the excitation energy and maintain optimal photosynthetic efficiency, higher plants and green algae have acquired

Published by the Molecular Plant Shanghai Editorial Office in association with Cell Press, an imprint of Elsevier Inc., on behalf of CSPB and CEMPS, CAS.

²School of Life Science, Southern University of Science and Technology, Shenzhen 518055, China

³State Key Laboratory of Membrane Biology, Beijing Advanced Innovation Center for Structural Biology, Beijing Frontier Research Center for Biological Structure, School of Life Sciences, Tsinghua University, Beijing 100084, China

⁴Cryo-EM Center, Southern University of Science and Technology, Shenzhen 518055, China

⁵Photosynthesis Research Center, Key Laboratory of Photobiology, Institute of Botany, Chinese Academy of Sciences, Beijing 100093, China

⁶These authors contributed equally to this article.

^{*}Correspondence: SenFang Sui (suisf@mail.tsinghua.edu.cn), Lixin Zhang (zhanglixin@henu.edu.cn)

the ability to perform state transitions, a short-term response that involves reversible changes in antenna cross-section of the PSs in state 1 and state 2 (Tikkanen et al., 2006). This process is controlled by the redox state of the plastoquinone (PQ) pool, and the reversible phosphorylation of LHCII trimers catalyzed by the chloroplast protein kinase STN7 and the phosphatase PPH1/TAP38 (Depege et al., 2003; Bellafiore et al., 2005; Pribil et al., 2010; Shapiguzov et al., 2010). In state 1, LHCII is mostly associated with the PSII core. Upon overexcitation of PSII, the PQ pool is reduced, and PQH2 docks to the Qo site of the cytochrome b₆f complex. This process activates the STN7 kinase and the subsequent phosphorylation of the N-terminal region of LHCII. Then the phosphorylated LHCII trimer migrates from PSII to PSI, triggering the transition from state 1 to state 2 and forming the PSI-LHCI-LHCII supercomplex with increased antenna cross-section and excitation energy transfer to PSI (Eberhard et al., 2008; Rochaix, 2013; Longoni et al., 2015). In contrast, when PSI is preferentially excited with far-red (FR) light, the PQ pool is oxidized, and STN7 is inactivated. The LHCII trimer is dephosphorylated by the PPH1/TAP38 phosphatase and then detaches from PSI and returns to PSII, thus restoring state 1 (Lemeille and Rochaix, 2010). In this way, the excitation energy is redistributed between PSI and PSII through the reversible binding of the LHCII trimer.

The structure of PSI-LHCI-LHCII from Zea mays (Zm), determined by cryoelectron microscopy (cryo-EM), revealed for the first time the architecture of the PSI-LHCI-LHCII supercomplex and in particular the recognition site between the LHCII trimer and the PSI core, where the PsaO subunit is essential for association of the LHCII trimer (Jensen et al., 2004; Pan et al., 2018). Recently, cryo-EM structures of Chlamydomonas reinhardtii (Cr) PSI-LHCI-LHCII revealed the binding of two LHCII trimers composed of four types of LhcbM proteins and the direct interactions of two LhcbM isoforms with the PSI core (Huang et al., 2021; Pan et al., 2021). These structural studies identified the docking sites of the LHCII trimer with PSI-LHCI. However, although the PSI-LHCI module in maize PSI-LHCI-LHCII (Pan et al., 2018) displays a similar architecture as the X-ray structures of higher-plant PSI-LHCI (Ben-Shem et al., 2003; Amunts et al., 2007; Mazor et al., 2015, 2017; Qin et al., 2015; Wang et al., 2021), the ST-induced conformational changes of PSI-LHCI and the resulting alterations of the excitation energy transfer (EET) pathways are largely unknown. Furthermore, genetic analyses of PSI mutants in Arabidopsis (Jensen et al., 2000, 2004; Varotto et al., 2002) and comparative analysis with the PSI-LHCI structure of Pisum sativum (Mazor et al., 2017) showed that, besides PsaL/PsaH/ PsaO, two additional subunits, Psal and PsaK, may also be involved in state transitions. However, no structural data are available for elucidating the molecular mechanisms of the action of Psal/PsaK subunits during state transitions in *Arabidopsis* or *P.* sativum and the nature of the dynamic conformational changes of the docking sites during state transitions.

In the present study, we isolated the PSI–LHCI (named PSI–LHCI-ST1) and PSI–LHCI–LHCII (named PSI–LHCI–LHCII-ST2) supercomplexes from *Arabidopsis* plants after they were treated with FR light (state 1 [ST1]) and white light (state 2 [ST2]), respectively. Structural comparisons of cryo-EM maps of PSI–LHCI-ST1 at 3.0 Å and PSI–LHCI–LHCII-ST2 at 2.8-Å resolution revealed a more compact PSI–LHCI architecture, besides the binding of

the LHCII trimer, and shorter Mg-to-Mg distances of the neighboring chlorophylls (Chls) located in the LHCI belt and the peripheral PSI subunits in ST2, which may contribute to enhance EET from the antenna to the PSI reaction center. Compared with ST1, the PsaA/PsaL/PsaK subunits undergo several conformational changes to facilitate the binding of PsaO in ST2, which completes the docking site of the LHCII trimer on the PSI-LHCI supercomplex. Combined with extensive genetic characterizations, we show that the mobile LHCII trimer steadily binds to PSI-LHCI through the newly identified PsaK-Lhcb1 and known PsaL/H/O-Lhcb2 interactions. Our work reveals dynamic structural rearrangements of PSI during transition from ST1 to ST2, broadening our understanding of state transitions in higher plants.

RESULTS

Identification of PSI-LHCI-LHCII-ST2 and PSI-LHCI-ST1 supercomplexes purified from light-stimulated *Arabidopsis* plants

To investigate the structural and functional correlations of the PSI-LHCI supercomplex during state transitions, we irradiated cultured Arabidopsis seedlings with FR light (730 nm, light-emitting diode) and white light separately (Supplemental Figure 1) which are known to induce ST1 and ST2, respectively (Bellafiore et al., 2005; Pribil et al., 2010; Shapiguzov et al., 2010, 2016; Wu et al., 2021). Blue native (BN) PAGE of the isolated thylakoid membranes revealed the presence of the PSI-LHCI-LHCII band in Arabidopsis irradiated with white light (Figure 1A). Then the PSI-LHCI-LHCII-ST2 and PSI-LHCI-ST1 supercomplexes were purified by clear native (CN)-PAGE and subsequent size exclusion chromatography (SEC) (Figure 1A and Supplemental Figure 2). Compared with PSI-LHCI-ST1, room-temperature absorption spectra of PSI-LHCI-LHCII-ST2 showed significantly higher absorption at 470 nm and 650 nm (Figure 1B and Supplemental Figure 3A). In addition to a lowtemperature fluorescence emission peak at 730 nm similar to that of PSI-LHCI-ST1, PSI-LHCI-LHCII-ST2 displayed an extra peak at 680 nm representing more Chl b in the purified PSI-LHCI-LHCII-ST2 (Figure 1C and Supplemental Figure 3B; Supplemental Table 1). A similar conclusion was reached from the low-temperature fluorescence excitation spectra, which showed higher peaks at 469 nm and 650 nm in the PSI-LHCI-LHCII-ST2 sample than that in PSI-LHCI-ST1 sample (Supplemental Figure 4). Consistently, the Chl a/b ratio (Ouyang et al., 2020) of PSI-LHCI-LHCII-ST2 was lower (7.7) compared with PSI-LHCI-ST1 (12.4) (Figure 1D). These values are close to the theoretical values calculated from the known PSI-LHCI-LHCII-ST2 structures in the PDB (Supplemental Table 2).

To further identify the protein components that contain more Chl b, the gel strips from native PAGE were analyzed with Coomassie brilliant blue (CBB) and silver staining using 2D PAGE. An extra spot at 25 kDa corresponding to Lhcbs was observed in the PSI-LHCI-LHCII-ST2 samples (Figure 1E and Supplemental Figure 5). Immunoblot assays further revealed that PSI-LHCI-ST1 only contains the PSI subunits (such as PsaA and Lhca1), whereas PSI-LHCI-LHCII-ST2 displays several extra bands, including Lhcb1 and Lhcb2, which contain more Chl b, and the

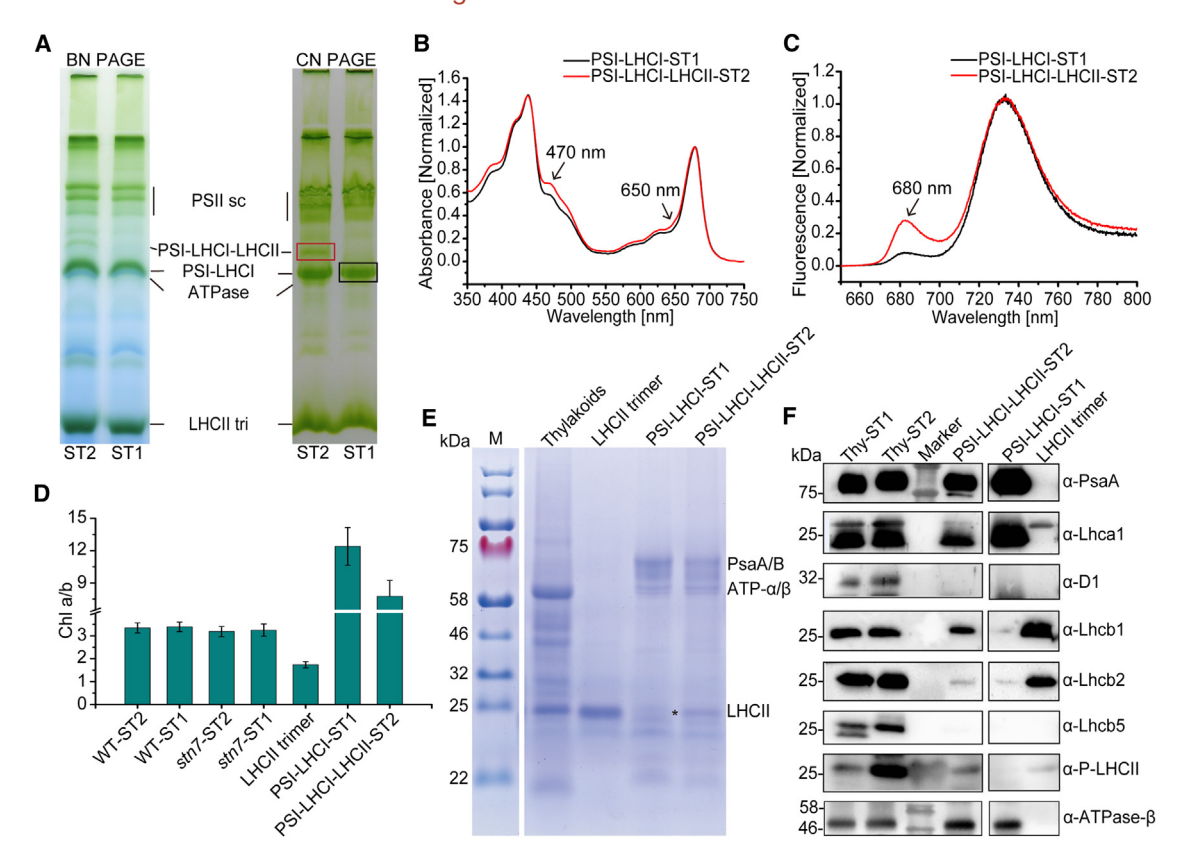


Figure 1. Isolation and characterization of the PSI-LHCI-LHCII-ST2 and PSI-LHCI-ST1 supercomplexes.

(A) Native PAGE analyses (left, BN PAGE; right, CN PAGE) of PS complexes from plants subjected to white light (ST2) and FR light (ST1) conditions. A 50- μ l sample (1.0 μ g Chl/ μ l) was loaded for each lane.

(B) Room-temperature absorption spectra of PSI-LHCI-ST1 and PSI-LHCI-ST2 obtained from SEC. The spectra were normalized at the maximum absorbance of PSI. The peaks at 470 nm and 650 nm are indicated by arrows, indicating that PSI-LHCI-LHCII in ST2 contains more ChI b (from LHCII) than the PSI-LHCI supercomplex in ST1.

(C) Low-temperature emission spectra (77 K) of PSI–LHCI-ST1 and PSI–LHCII-ST2 obtained from SEC upon excitation of Chl a at 435 nm. The spectra were normalized to the absorbance of PSI–LHCI at 730 nm.

(D) Chl a/b ratios of PSI-LHCI-ST1, PSI-LHCII-ST2, the LHCII trimer, and thylakoid membranes of the WT and stn7 in ST1 and ST2. Data are the means \pm SEM (n = 5 biological replicates).

(E) SDS-PAGE analysis of the purified PSI-LHCI-ST1, PSI-LHCI-LHCII-ST2 and LHCII trimer, and thylakoid membranes. A 15-μI sample (1.0 μg protein/μI) was loaded on each lane. The band of the LHCII trimer at 25 kDa is marked with a star.

(F) Immunoblot analysis of PSI-LHCI-ST1, PSI-LHCI-LHCII-ST2 and the LHCII trimer, and thylakoid membranes in ST1 and ST2 with antibodies of PSI subunits (PsaA and Lhca1), PSII subunits (D1, Lhcb1, and Lhcb5), and phosphothreonine antiserum. A $10-\mu l$ sample ($1.0~\mu g$ protein/ μl) was loaded on each lane.

phosphorylated LHCII subunits (Figure 1F). Each subunit of the PSI-LHCI-LHCII-ST2 and PSI-LHCI-ST1 supercomplexes was further examined by mass spectrometry (MS), which showed that the LHCII peptides derived from PSI-LHCI-LHCII-ST2 could arise from the isoforms Lhcb1.1-Lhcb1.5 and Lhcb2.1-Lhcb2.3 (Supplemental Table 3).

Dynamic conformational changes of PSI-LHCI during state transitions

To elucidate the structural dynamics during state transitions, the vitrified PSI-LHCI-LHCII-ST2 and PSI-LHCI-ST1 were subjected to single-particle cryo-EM analyses. The final reconstructed cryo-EM map of PSI-LHCI-LHCII-ST2 at 2.8-Å, the LHCI belt at 3.2-Å, and the LHCII trimer at 3.1-Å resolution enabled us to build an accurate model of the transmembrane (TM) helices with the side chains and all of the cofactors (Figure 2A and 2B and Supplemental Figures 7 and 8; Supplemental Tables 4 and 5).

The composition and overall structure of PSI-LHCI-ST1 at 3.0-Å resolution resembles the PSI-LHCI module of PSI-LHCI-LHCII-ST2 (Figure 2C and 2D and Supplemental Figures 6 and 9; Supplemental Tables 4, 6, and 7). The refined PSI core contains 12 subunits (PsaA-PsaL), but PsaN was absent in these two structures (Figure 2). Surprisingly, the PsaN subunit was detected by immunoblot analysis in all eluates of the SEC-purified samples at 0 and 24 h (Supplemental Figure 10A). Although the PSI activity in the *psan* mutant was lower than in the wild-type (WT) or *stn7* mutant (Supplemental Figure 10B-10E), the BN-PAGE and ChI fluorescence analyses revealed normal state transitions in the *psan* mutant (Supplemental Figure 11A and 11B).

Superimposition of the PSI-LHCI-ST1 and PSI-LHCI-LHCII-ST2 structures gives root-mean-square deviations of 0.269 at the PSI core and 0.439 at the four LHCI subunits. Compared with PSI-LHCI-ST1, the overall architecture of the PSI-LHCI module

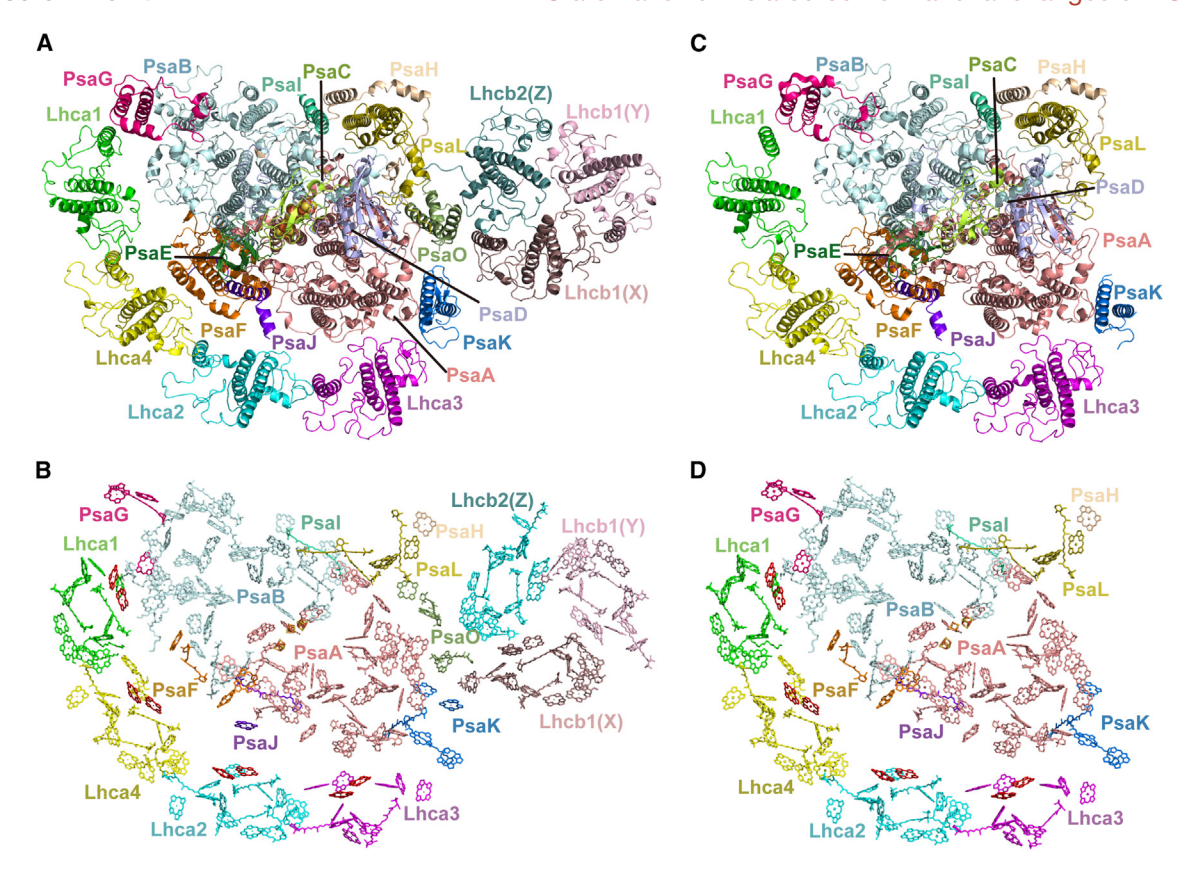


Figure 2. Overall architecture and ChI distributions of the PSI-LHCI-LHCII-ST2 and PSI-LHCI-ST1 supercomplexes.

Shown is an overview of the protein subunits (top) and Chl arrangement (bottom) of PSI-LHCI-LHCII-ST2 (A and B) and PSI-LHCI-ST1 (C and D) supercomplexes on the stromal side. All subunits are shown as cartoons, and the Chls are shown as stick models with the same color pattern as the subunits. Two red form Chl a in each Lhca subunit are shown in red. Two red form Chls a in each Lhca subunit are shown as sphere models. Lhca1, green; Lhca2, cyan; Lhca3, magenta; Lhca4, yellow; PsaA, salmon; PsaB, pale cyan; PsaC, limon; PsaD, light blue; PsaE, forest; PsaF, orange; PsaG, hot pink; PsaH, wheat; PsaI, green cyan; PsaJ, purple blue; PsaK, marine; PsaL, olive; PsaO, smudge; Lhcb2, light teal; Lhcb1(X), dirty violet; Lhcb1(Y), light pink; SF4, spheres.

had a more compact conformation in the PSI-LHCI-LHCII-ST2 structure, characterized by shifts of various degrees of the four peripheral LHCI subunits toward the PSI core (Figure 3A-3F). At the LHCIs belt end, two helices of the PsaK subunit slightly moved toward PsaA in ST2, but not those of the PsaG subunit (Figure 3B) and 3C), which may be due to the binding of PsaO and the LHCII trimer on the PsaK side in ST2 (see below). At the interfaces between the peripheral subunits and the PSI core, several conformational changes were observed during state transitions. In the interface of PsaG-Lhca1, the movement of the helixes leads to shorter distances between L138, P139, E145, F146, and Chl a603 of Lhca1 with L78, Y145, I146, N152, and Chl a201 of PsaG in ST2, respectively (Figure 4A and Supplemental Figure 12). Similar conformational changes occur at A137/S138_{Lhca4}-W229_{Lhca1}, S140_{Lhca4}-G234_{Lhca1}, H224_{Lhca1}-Chl *a612*_{Lhca1}, and F143_{Lhca4}-Chl b606_{Lhca4} in the interface of Lhac1/Lhca4 (Figure 4B and Supplemental Figure 13) Additionally, the N-terminal loop (13-40) of PsaA inserted into the gap between Lhca3/PsaJ and PsaA in ST2 strengthens their interactions with E85_{Lhca3}-L13_{PsaA}, G86/G88_{Lhca3}-V14_{PsaA}, G89_{Lhca3}-R16_{PsaA}, L4_{PsaJ}- $F23_{Lhca3}$, $D3_{PsaJ}$ - $E24_{Lhca3}$, $Y7_{PsaJ}$ - $W26_{Lhca3}$, and $T6_{PsaJ}$ -A27_{Lhca3} (Figure 4C and Supplemental Figure 14). These conformational changes result in a more compact conformation of PSI-LHCI in ST2, which may enhance the interactions between the LHCI subunits and the PSI core.

Specific interactions enhance the binding of PsaO and the LHCII trimer to PSI-LHCI

MS analyses showed that the mobile LHCII trimers could be organized by Lhcb1.1-Lhcb1.5 and Lhcb2.1-Lhcb2.3 (Supplemental Table 3). To examine the composition of the LHCII trimer in the PSI-LHCI-LHCII-ST2 supercomplex, the cladogram of Lhcb1 and Lhcb2 from A. thaliana, Z. mays, and C. reinhardtii was established with a maximum-likelihood tree using MEGA software. According to the amino acid sequence alignment, the Lhcb proteins were divided into four groups (Supplemental Figure 15A). Specifically, AtLhcb2 contains N-terminal residues strictly conserved with ZmLhcb9 (also named Lhcb2 in maize PSI-LHCI-LHCII) (Pan et al., 2018), and these Lhcb isoforms all belong to group II in cladogram analyses (Supplemental Figures 15B and 16-18). According to the 3.1-Å local resolution of the LHCII trimer and sequence analyses, the Lhcb monomer close to the PsaL/PsaO subunits was assigned as the mature Lhcb2, and the other two Lhcb monomers belonged to Lhcb1 proteins (Figure 2 and Supplemental Figure 19).

In ST2, the N terminus of Lhcb2, including Arg1, Arg2, and the phosphorylated threonine (pT3), is bound at the PSI–LHCI–LHCII interface and forms extensive hydrogen-bonding interactions with amino acid residues from the PsaL/H subunits of PSI–LHCI (Figure 5A). Superposition of the PSI–LHCI–ST1 and PSI–LHCI–LHCII-ST2

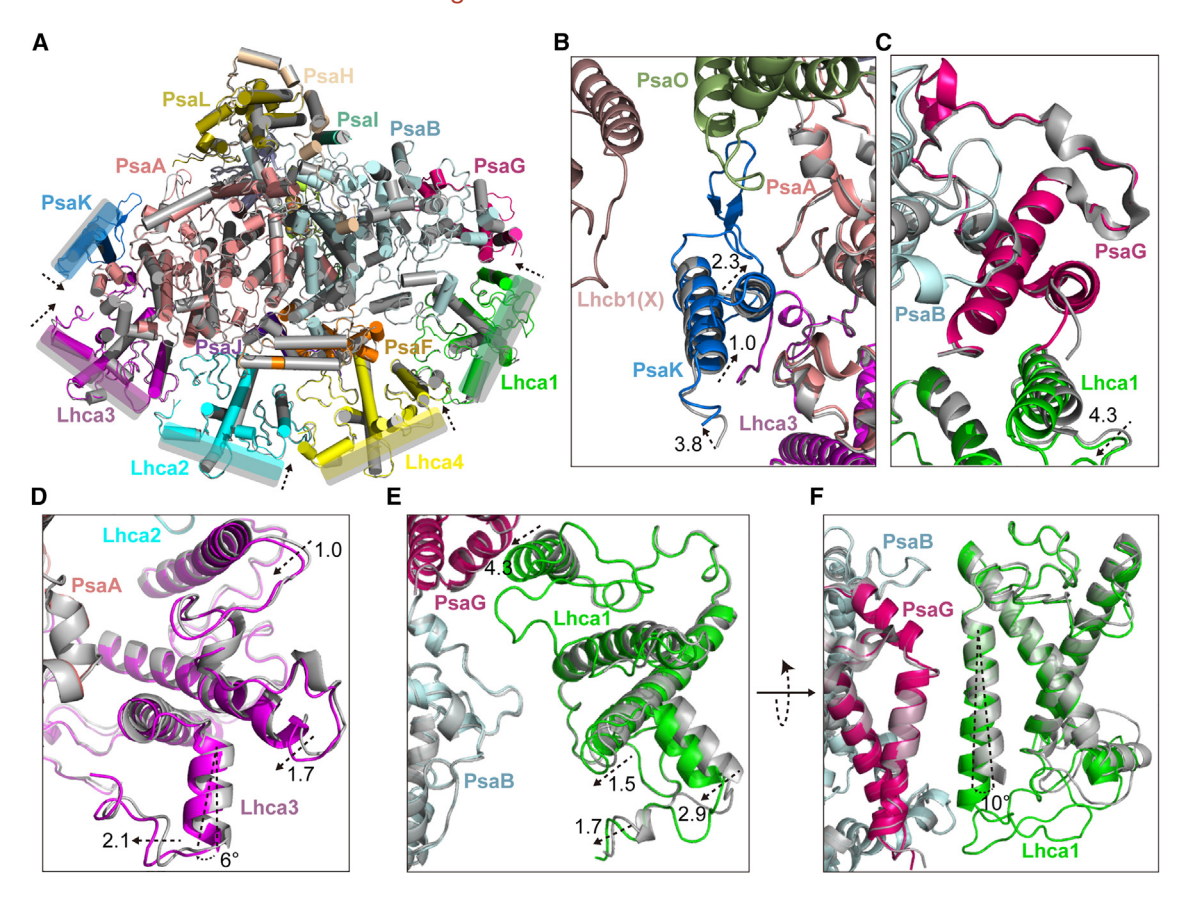


Figure 3. Conformational changes of the PSI-LHCI supercomplex during state transitions.

(A) Superposition of PSI-LHCI-ST2 (iridescence) and PSI-LHCI-ST1 (gray) supercomplexes at the PSI core; the structures are shown as cartoon models. Longitudinal and horizontal dimensions of PSI from a top view are indicated on the lumenal side. The periphery of each Lhca subunit is shown as a shadow with its corresponding color. The dashed arrows indicate the conformational shifts (Å) of Lhcbs during the transition from ST1 to ST2. The rotation of helixes of Lhca3 and Lhca1 is indicated in degrees.

(B–F) Conformational changes (dashed arrows) of the PsaK (B), PsaG-Lhca1 interface (C), Lhca3 (D), and Lhca4 (E and F) during state transitions. The secondary structures from PSI–LHCI–ST2 (iridescence) and PSI–LHCI–ST1 (gray) supercomplexes are shown as cartoons and labeled.

structures revealed several conformational changes of Glu75, Ser80, Ser89, Thr170, Thr172, and Arg174 from PsaL and Ser76 from PsaH (Figure 5A and Supplemental Figure 20), indicating that the PsaL and PsaH subunits underwent structural rearrangements to strengthen the association of the LHCII trimer during transition to ST2. The subunit PsaO was absent in PSI-LHCI-ST1 but present in the PSI-LHCI-LHCII-ST2 supercomplex (Figure 2), indicating that this subunit plays an essential role as "molecular glue" that bridges the contacts between the LHCII trimer and the PSI core (Figure 5B and 5C). At the PSI-LHCI-LHCII interface, the N-terminal regions of PsaO (O loop, E53-D60) and Lhcb2 (b2 loop, R1-W12) were parallel and inserted into PsaL loops, where they formed tight interactions within these three subunits on the stromal side (Figure 5A and 5B). Superposition of PSI-LHCI-ST1 and PSI-LHCI-LHCII-ST2 indicates that a flexible loop of PsaA (A loop, A324-L338) underwent a remarkable conformational change to accommodate Chl a845_{PsaA} in ST2, which favors the binding of PsaO through several hydrophobic interactions (L57/I130/K133/G134_{PsaO}-Chl a845_{PsaA}) and hydrogen bonds (T126/Q129_{PsaO}-Chl a845_{PsaA}) (Figure 5B and 5B-5I and Supplemental Figure 21). Consistently, the N terminus of PsaL (L-N loop) moved to the PSI core and tied up with the flexible loop of PsaA by $Q60_{PsaL}$ -P239 $_{PsaA}$ interaction in ST2. On the lumenal side, conformational changes of W483/

N486/Chl $a837_{PsaA}$ promoted the interactions with I80/L106/T107_{PsaO} (Figure 5C and Supplemental Figure 22). Furthermore, the β -hairpin (G71–T95) of PsaK that disappeared in the PSI–LHCI-ST1 structure stretched to PsaO and contacted it through the interactions A82_{PsaK}–Chl $a203_{PsaO}$ in ST2 (Figure 5B and 5B-II and Supplemental Figure 21). Compared with Cr PSI–LHCI-LHCII, which forms fewer PsaK–Lhcb1 contacts, the L72/P74 in the β -hairpin stabilized the orientation of Chl $a206_{PsaK}$, allowing the latter and R85 together to interact with Nex618 of Lhcb1 on the stromal side (Figure 5B and Supplemental Figure 23), which provided another docking site for Lhcb proteins that contribute significantly to stabilizing the binding of the LHCII trimer.

To further investigate the physiological function of the PsaK subunits during state transitions, mutants deficient in the docking subunits were generated using the CRISPR-Cas9 system (Supplemental Figure 24), and their phenotypes were characterized. Compared with the stn7 mutant and WT, the maximum absorbance change of P700 (Δ P700 $_{max}$) was conspicuously decreased in psak, psal, and psao, but it was normal in psah (Figure 5D). Based on the state transition fluorescence assay, the adult psak and psah plants were partially deficient in state transitions, whereas the psal and

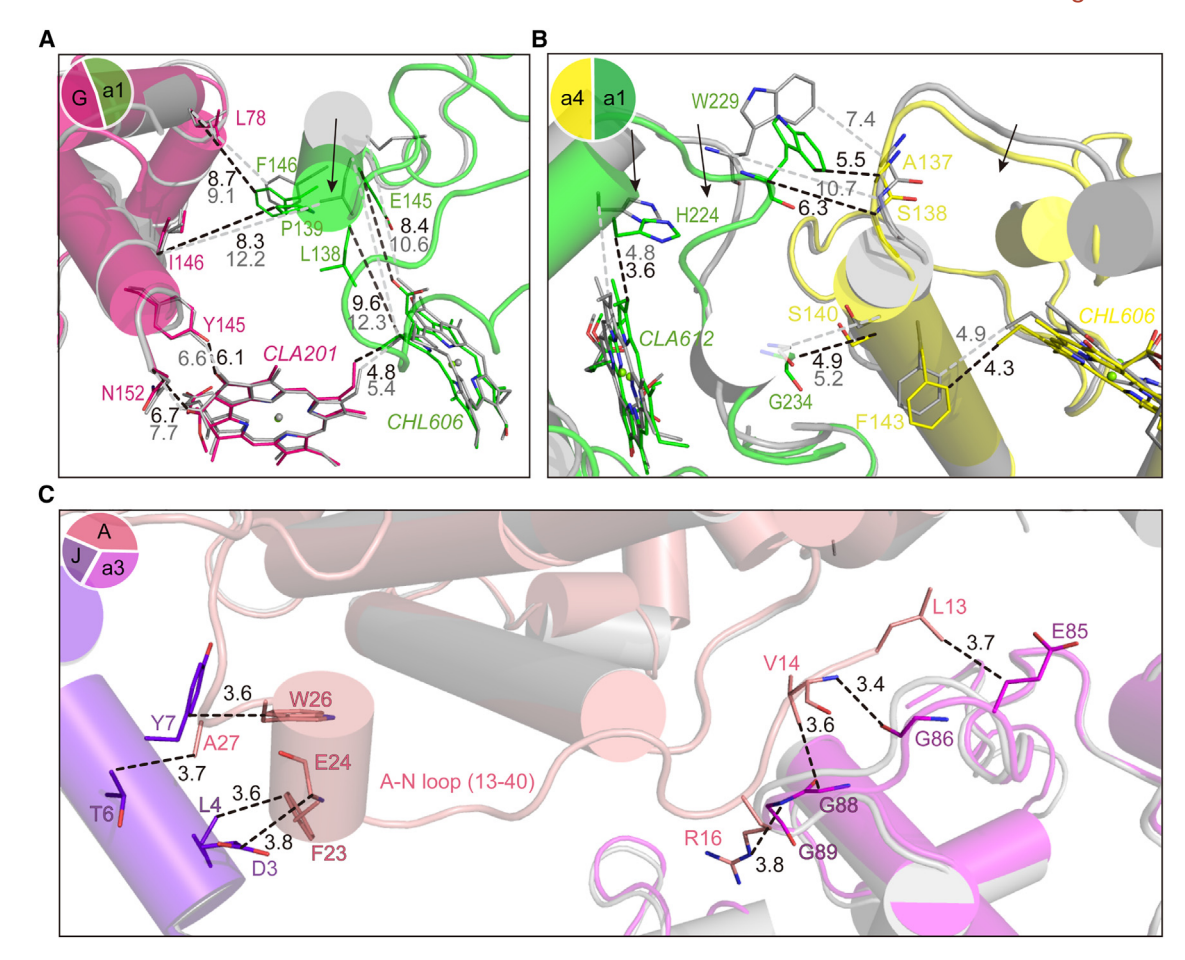


Figure 4. Conformational changes of the residues located at the interface between LHCls and the PSI core during state transitions. The structures of PSI-LHCI-ST2 (iridescence) and PSI-LHCI-ST1 (gray) supercomplexes are superimposed at the PSI core. The key amino acids involved in the subunit interactions are shown as stick models. The arrows indicate the conformational shifts of subunits during the transition from ST1 to ST2. The residues at the interfaces between Lhca1 and PsaG (A), Lhca1 and Lhca4 (B), and PsaJ, Lhca3, and PsaA (C) are shown as stick models with respective colors. Distances (Å) between two main-chain or aromatic atoms (A and B) and interfacial atoms (C) of the key residues in ST2 and ST1 are shown as black and gray dashed lines, respectively.

psao mutants had a similar phenotype as stn7 (Figure 5E). Although the quantum yields of PSII (Fv/Fm fluorescence) and the STN7-dependent phosphorylation of LHCII of these mutants were similar to WT, the PSI-LHCI-LHCII band in BN-PAGE was undetectable in the psak, psal, psah, and psao strains (Figure 5E and Supplemental Figure 25), indicating that the deficiency of state transitions in psak, psal, psah, and paso resulted from the absence of the PSI-LHCI-LHCII-ST2 supercomplex rather than damage of the PSII supercomplex or lack of STN7 activity. Therefore, these structural and genetic analyses demonstrate that the second docking site, PsaK, as well as PsaL are not only essential for state transitions but also necessary for maintaining the intact activity of PSI, whereas PsaH probably only participates in the binding of the LHCII trimer to PSI during transition from ST1 to ST2.

Alterations of the potential energy transfer pathways during state transitions

During state transitions, reorganization of the light-harvesting antenna allows dynamic regulation of EET. According to the previously depicted EET pathways of the higher-plant PSI-LHCI supercom-

plex (Ben-Shem et al., 2003; Amunts et al., 2007; Mazor et al., 2015, 2017; Qin et al., 2015; Wang et al., 2021), several plausible EET pathways were identified based on the cryo-EM densities of PSI-LHCI-ST1 and PSI-LHCI-LHCII-ST2 (Figure 6). Upon preferential excitation of PSII relative to PSI, the extra LHCII trimer docks at the subunits PsaL/H/O/K, acting as a peripheral antenna of PSI-LHCI. Because Chl b has a higher energy level than Chl a (Qin et al., 2015), Chl a202 $_{\rm PsaO}$ may gather excitation energy from the three Chlb clusters and other Chla molecules in the LHCII trimer via Chl a611/a614_{Lhcb2}. Strikingly, compared with ZmPsaO, a newly identified Chl a201 of AtPsaO transfers the energy from Chl $a202_{PsaO}$ (Mg to Mg, 14.4 Å) to Chl $a304_{PsaL}$ (Mg to Mg, 15.8 Å) and/or Chl a839_{PsaA} (Mg to Mg, 19.4 Å) (Figure 6A). Due to the cross-road localization of PsaK, Chl a203 may serve as a bridge for connecting Chl b608_{Lhcb1} (Mg to Mg, 18.7 Å) and Chl a818_{PsaA} (Mg to Mg, 11.4 Å), which serves as another energy transfer route between LHCII and the PSI core (Figure 6). Upon transition from ST1 to ST2, these potential EET pathways mediate energy transfer from the LHCII trimer to PSI-LHCI.

As the main antenna of PSI-LHCI, four LHCI subunits form two heterogeneous dimers, Lhca1-Lhca4 and Lhca2-Lhca3, which

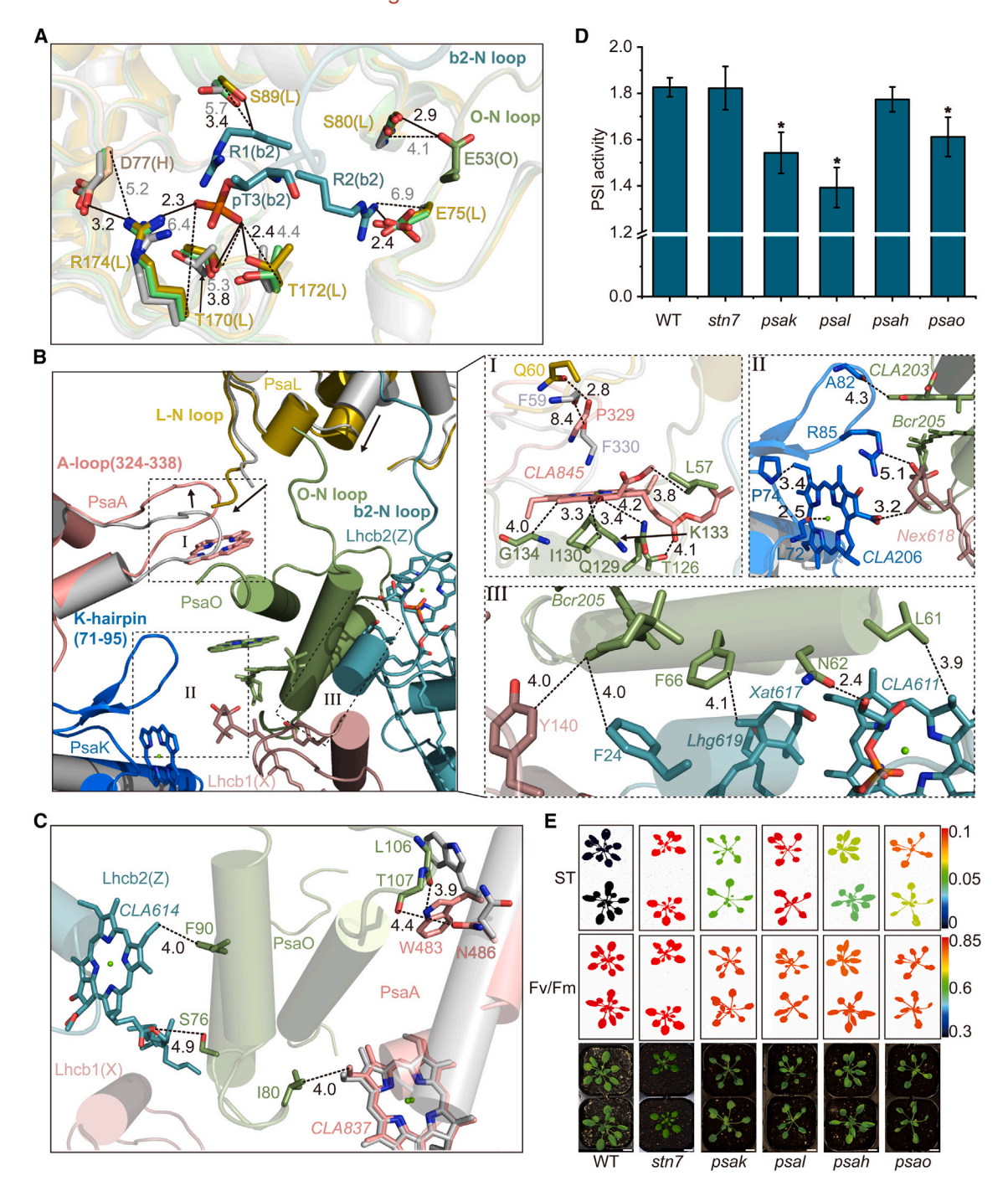


Figure 5. Dynamic conformational changes contribute to the assembly of PsaO and the LHCII trimer in the PSI-LHCI-LHCII-ST2 supercomplex.

(A) Superposition of PSI-LHCI-ST2 (iridescence), PSI-LHCI-ST2 (gray green), and PSI-LHCI-ST1 (gray) supercomplexes. Shown are interactions among PsaL, PsaH, PsaO, and the N terminus of Lhcb2 (including the phosphorylated T3). The key amino acid residues during state transitions are shown as stick models. The full lines with black numbers indicate the hydrogen bonds between Lhcb2/PsaO and the PsaL/PsaH in the interfaces. The dashed lines with gray numbers indicate the distances between Lhcb2/PsaO and the main-chain atoms of PsaL/PsaH.

(B) Dynamic conformational changes of PsaA/PsaL/PsaK in PSI-LHCI-ST1 (gray) and PSI-LHCI-LHCII-ST2 (iridescence) affect the binding of PsaO and the LHCII trimer on the stromal side. The details of interactions of PsaA-PsaL-PsaO (I), PsaK-PsaO-Lhcb1 (II), and PsaO-Lhcb1-Lhcb2 (III) are shown within dashed boxes. Their interactions are indicated with dashed lines.

(C) Interfaces among PsaA/PsaL/PsaK/PsaO-Lhcb2/Lhcb1 in PSI-LHCI-ST1 (gray) and PSI-LHCI-LHCII-ST2 (iridescence) on the lumenal side.

(legend continued on next page)

also absorb and transfer light energy to the PSI core through multiple potential EET pathways. Based on the Mg-to-Mg distances of the interfacial Chls, the Chls in Lhca1-PsaB and Lhca3-PsaA could form the main EET routes (Figure 6, red arrows), including a603_{Lhca1}-a841_{PsaB}, *b*606_{Lhca1}-*a*201_{PsaG}-*a*835_{PsaB}, $b608_{Lhca1}$ - $a822_{PsaB}$ in Lhca1-Lhca4 and $a602_{Lhca3}$ - $a811_{PsaA}$ and a605_{Lhca3}-a817_{PsaB} in Lhca2-Lhca3. Compared with the main EET routes, energy transfer between Lhca2-PsaA and Lhca4-PsaB is mediated by a101_{PsaJ} and a302/303_{PsaF} over longer distances (Figure 6, gray shadow). Concomitant with the conformational changes of the protein subunits, the Chl distribution of PSI-LHCI was also altered during state transitions. Chls in peripheral subunits underwent changes in location during state transitions, resulting in shortened distances of the nearestneighboring Chl pairs in the EET pathway (Figure 6). Based on the reported EET routes (Ben-Shem et al., 2003; Amunts et al., 2007; Mazor et al., 2015, 2017; Qin et al., 2015; Wang et al., 2021), most Mg-Mg distances of Chl-Chl pairs in LHCs were shorter in ST2 than in ST1, and when the total distance was calculated, we found that it had decreased by 4.5 Å (stromal side) and 3.9 Å (lumenal side) in ST2 (Supplemental Table 8). These Chl rearrangements could enhance the EET efficiency from the four LHCIs and peripheral subunits to the PSI core in ST2.

To assess PSI performance during state transitions, we measured the P700 oxidation rate of the purified PSI–LHCI-ST1 and PSI–LHCI-LHCII-ST2 supercomplexes. Using thylakoid membranes as a control, PSI–LHCI-LHCII-ST2 showed a relatively faster P700 oxidation rate than PSI–LHCI-ST1 (Supplemental Figure 26A; Supplemental Table 9), indicating a higher electron transport efficiency and/or larger light-harvesting cross-section of PSI–LHCI upon transition from ST1 to ST2 (Cao et al., 2020). In contrast, the P700 reduction rate was the same for the two supercomplexes (Supplemental Figure 26B). Taken together, these results indicate that association of the LHCII trimer as well as the dynamic conformational changes and rearrangements of Chls during state transitions are necessary for enhancing the EET efficiency from the peripheral antenna proteins to the PSI core.

DISCUSSION

State transitions play important roles in the light acclimation of oxygenic photosynthetic organisms, in which the excitation energy is redistributed between PSI and PSII through reversible binding of the phosphorylated LHCII trimer to the PSI–LHCI supercomplex (Eberhard et al., 2008; Rochaix, 2014). In this work, we determined the cryo-EM structures of PSI–LHCI-ST1 and PSI–LHCI–LHCII-ST2 from A. thaliana and found that conformational changes of PsaA/PsaL accommodate the assembly of PsaO, further strengthening the binding of the LHCII trimer. In addition to the known PsaL/PsaH subunits for Lhcb2 binding, PsaK acts as a novel docking site for Lhcb1 and forms an extra EET route from LHCII to PSI–LHCI. Structural comparisons demonstrated that PSI-LHCI adopts a more compact configura-

tion with shorter Mg-to-Mg distances of the Chls between the LHCl belt and the PSI core in state 2, which is expected to enhance the EET from the peripheral antenna proteins to the PSI-LHCl reaction center.

In the PSI-LHCI-LHCII-ST2 structure, the mobile LHCII trimers could arise from Lhcb1 and/or Lhcb2. Because the Lhcb2 knockout mutant of *Arabidopsis* is deficient in state transitions, Lhcb2, but not Lhcb1, plays an essential role in state transitions (Pietrzykowska et al., 2014). Previous Phos-tag and biochemical analyses revealed that Lhcb2 was fully phosphorylated in the PSI-LHCI-LHCII supercomplex, whereas phosphorylated Lhcb1 was excluded (Leoni et al., 2013; Crepin and Caffarri, 2015; Longoni et al., 2015). Based on the close cladogram relationship (Supplemental Figures 15–17), cryo-EM density (Supplemental Figure 19), and strictly conserved conformation of the N terminus of AtLhcb2 with ZmLhcb9 (also named Lhcb2) and CrLhcbm1 (Supplemental Figure 15), the three Lhcb monomers of the LHCII trimer in our structure were recognized as phosphorylated Lhcb2 and two dephosphorylated Lhcb1 proteins. This ratio of Lhcb1:Lhcb2 (2:1) in the mobile LHCII trimer is consistent with previous studies (Crepin and Caffarri, 2015; Su et al., 2017; Pan et al., 2018). In CrPSI-LHCI-LHCII (Pan et al., 2021), the S chain (corresponding to Lhcb2) was assigned as CrLhcbm1, which was the only Lhcbm that contains an N terminus identical to plant Lhcb2 (1-RRpTVK-5). Interestingly, the S chain of another CrPSI-LHCI-LHCII structure (Huang et al., 2021) was annotated as CrLhcbm4 (similar to AtLhcb1, which contains 1-RKpTVAK-6 at the N terminus) based on the reported genetic analyses showing that deletion of Lhcbm1 does not affect state transitions in Cr (Elrad et al., 2002; Ferrante et al., 2012; Drop et al., 2014).

PsaN, a membrane-extrinsic subunit, locates at the PSI-LHCI interface on the luminal side (Pan et al., 2018). Notably, although the PsaN subunit was missing in the PSI core of the PSI-LHCI-ST1 and PSI-LHCI-LHCII-ST2 supercomplexes compared with maize PSI-LHCI-LHCII (Pan et al., 2018), it does not affect state transitions or the assembly of the PSI supercomplex (Figure 2 and Supplemental Figure 11A and 11B). Similarly, due to the weaker contacts between PsaN and the PSI core, loss of the PsaN subunit was also observed in previous structural studies of the PSI-LHCI complexes from pea (Mazor et al., 2015, 2017; Qin et al., 2015; Wang et al., 2021) and green algae (Qin et al., 2019; Su et al., 2019; Suga et al., 2019; Huang et al., 2021; Pan et al., 2021). Furthermore, P700 absorbance measurements indicated that PSI activity in the psan mutant was lower than in the WT or stn7 mutant (Supplemental Figure 10B-10D), indicating that the PsaN subunit is part of the PSI-LHCI supercomplex but not necessary for state transitions in Arabidopsis.

Superposition of our PSI-LHCI-ST1 and PSI-LHCI-LHCII-ST2 structures revealed apparent conformational changes of PSI-

⁽D) P700 absorbance in WT, stn7, psak, psal, psah, and psao was measured after dark adaptation for 30 min. The photosynthetic activity of PSI is indicated by the maximum change of the P700 curve (Δ P700_{max}). Data are the means \pm SEM (n=3 biological replicates). The statistical significance between three means of measurements was determined using Student's t-test; p < 0.01 or p < 0.05.

⁽E) Bright-field images. Chl fluorescence, and state transition fluorescence in the WT, stn7, psak, psal, psah, and psao (25-day adult plants in soil) were measured after dark adaptation for 30 min. False-color scale of ST fluorescence: black/dark blue represents normal state transition, and red indicates deficient state transition. Scale bars, 1.0 cm.

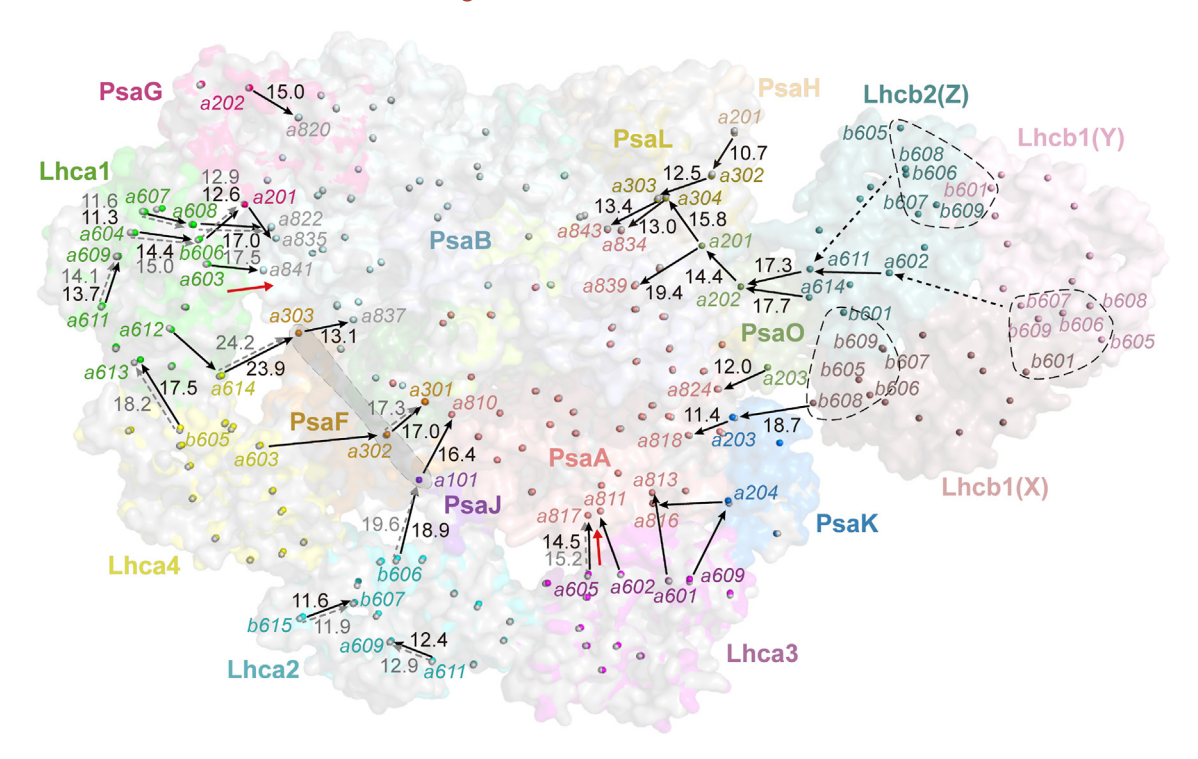


Figure 6. Plausible energy transfer pathways of the PSI-LHCI supercomplex in state transitions.

Shown are Chl distributions and possible excitation energy transfer (EET) pathways within the superimposed PSI–LHCI–LHCII-ST2 (iridescence) and PSI–LHCI-ST1 (gray). The protein subunits and the Mg atoms of Chls are shown as a transparent surface and sphere models, respectively. The Mg-to-Mg distances between the adjacent interfacial Chls are shown as numbers (Å). Black solid arrows, EET in ST2; gray dashed arrows, EET in ST1; black dashed arrows, feasible EET; red arrows, main EET directions; dashed irregular circles, clusters of Chl b; gray shadow, Chls of PsaF and PsaJ.

LHCI during state transitions. First, the interactions between LHCIs and the PSI core were tighter, forming a more compact overall architecture of PSI-LHCI in PSI-LHCI-LHCII-ST2 than in PSI-LHCI-ST1 (Figures 3 and 4). This may be a structural adaptation of PSI-LHCI to facilitate the interactions between peripheral antennas and the PSI core and the EET between them (Caspy et al., 2021). Interestingly, another PSI module without the LHCII trimer (PSI-LHCI-ST2) was separated from the particles of an ST2 sample and reconstructed at 2.8-Å resolution (Supplemental Figure 7). The origin of PSI-LHCI-ST2 may be attributed to 1) the disassembly of the LHCII trimer from PSI-LHCI-LHCII-ST2 during purification and/or vitrification of cryosample preparation or 2) cross-contamination of the PSI-LHCI-ST2 band close to the PSI-LHCI-LHCII-ST2 band in CN-PAGE (Figure 1A). Comparison of the PSI-LHCI-ST2 and PSI-LHCI-LHCII-ST2 structures showed the same conformation of the overall PSI-LHCI module (Supplemental Figure 27). In particular, some residues of the PsaL/PsaH subunits located at the interface with Lhcb2 have moved slightly compared with PSI-LHCI-LHCII-ST2 (Figure 5A), which may be due to the dissociation of the LHCII trimer.

Second, similar to ZmPSI-LHCI-LHCII and CrPSI-LHCI-LHCII (Pan et al., 2018, 2021; Huang et al., 2021), the subunit PsaO was present in the PSI-LHCI-LHCII-ST2 supercomplex but not in the PSI-LHCI-ST1 supercomplex of Arabidopsis (Figure 2). Further analysis of PSI-LHCI-LHCII-ST2 particles identified another supercomplex that contains the entire PSI-LHCI-ST2 and partial electron densities of the PsaO subunit (named PSI-LHCI-PsaO_{par}-ST2) (Supplemental Figure 28), but this structure

was not present in ST1 samples. Interestingly, the PsaO subunit was found in PSI-LHCI structures from the red alga Cyanidioschyzon merolae and green alga Dunaliella Salina under normal conditions (Pi et al., 2018; Caspy et al., 2020), but not found in pea (Ben-Shem et al., 2003; Amunts et al., 2007; Mazor et al., 2015, 2017; Qin et al., 2015; Wang et al., 2021). Moreover, the 2D PAGE assay from native PAGE showed that PsaO is present in the PSI-LHCI and PSI-LHCI-LHCII supercomplexes (Supplemental Figure 29). Thus, these analyses imply that PsaO is loosely bound to the PSI core in ST1 and may be lost during sample preparation, while conformational changes of other PSI subunits (PsaA, PsaL, and PsaK) and the binding of LHCII further stabilize its binding in ST2. In PSI-LHCI-LHCII-ST2, the large loop of PsaA turned toward the stromal side and was anchored by the N-terminal loop of PsaL moving in the opposite direction, which accommodates the binding of PsaO with the extensive interactions between PsaO and Chl a845_{PsaA} (Figure 5B). On the contrary, this PsaA loop obstructed the position of Chl a845 in the PSI-LHCI-ST1 structure. Similarly, the helices and β-hairpin shifts of PsaK favored the binding of PsaO in ST2. Notably, PsaG, another subunit that is located at the two ends of the LHCIs belt, showed no significant changes (Figure 3A-3C). This difference is consistent with the previous speculation based on the structural analysis of P. sativum PSI-LHCI supercomplex (Mazor et al., 2017). Therefore, the PsaA/ PsaL/PsaK subunits undergo several conformational changes to strengthen the binding of PsaO, indicating that the assembly of PsaO and the LHCII trimer to the PSI core act synergistically in ST2. Two possibilities can be envisaged concerning the mechanisms for inducing conformational changes of PSI-A/K/L: 1) the

binding of LHCII trimer induces conformational changes of PSI-A/K/L, which facilitate the accommodation of LHCII, or 2) light changes may induce several post-translational modifications of PSI subunits, such as phosphorylation and acetylation, resulting in conformational changes or rearrangement of photosynthetic proteins (Koskela et al. 2018, 2020).

Third, the residues of the PsaL/PsaH subunits exhibit more flexible conformations during state transitions (Figure 5A), which shapes a feasible binding environment for Lhcb2. On the other side, the stretched hairpin loop and Chl a206 of PsaK offer a second docking site for the LHCII trimer (Figure 5B and 5C). Thus, the PsaL/PsaH-Lhcb2 and PsaK-Lhcb1 interactions together strengthen the association of LHCII trimers with PSI-LHCI during state transitions in higher plants. Interestingly, a recent cryo-EM structure of PSI-LHCI-LHCII-Lhcb9 from the moss Physcomitrium patens (Pp) shows that PsaK mediates the EET from Lhcbm2b (the same localization of AtLhcb1(X) in the LHCII trimer) and Lhcb9 (a unique moss subunit that bridges the second LHCI belt with LHCII and the PSI core) to PsaA (Zhang et al., 2023), indicating a conserved function of PsaK in this respect from moss to higher plants. Unlike the psal, psao, and psak mutants, psan only showed decreased PSI activity, and psah was only deficient in state transition fluorescence (Figure 5D and 5E and Supplemental Figure 25), indicating that these two phenotypes are independent and that PsaH is not required for the PSI photochemical activity, although it is essential for state transitions. The latest PSI-LHCI structure in Cr (Naschberger et al., 2022) showed that the subunit PsaH is absent in the PSI-LHCI dimer but present in the CrPSI-LHCI-LHCII supercomplex (Huang et al., 2021; Pan et al., 2021). This is consistent with the role of PsaH in green algae and plants to prevent the formation of PSI-LHCI dimers or trimers (cyanobacteria that have a PSI core trimer lack of PsaH) and in its role for docking of the LHCII trimer(s) during state transitions (Mazor et al., 2013).

Last, the positions of Chls involved in EET routes from the four LHCI and peripheric subunits to the PSI core move during state transitions (Figure 6; Supplemental Table 9), suggesting that these pigment rearrangements facilitate transition from ST1 to ST2. Compared with the maize PSI-LHCI-LHCII structure (Pan et al., 2018), a newly identified Chl a201_{PsaO} could receive the excitation energy from Chl a202_{PsaO} that acts as a bridge for EET between the LHCII trimer and the PSI core via two close Chls, Chl a611 and a614 of Lhcb2, on the stromal and lumenal side, respectively. Interestingly, the Mg-to-Mg distances of Chl $a611_{Lhcb2}$ -Chl $a202_{PsaO}$ and Chl $a614_{Lhcb2}$ -Chl $a202_{PsaO}$ are shorter in Arabidopsis than in maize, which may be due to the flatter TM plane in the former (Supplemental Figure 30A-30C). On the side view, the relative angle between the TM planes of the LHCII trimer and PSI-LHCI in PSI-LHCI-LHCII-ST2 is decreased to 5° compared to 10° in the maize PSI-LHCI-LHCII structure. A possible reason is that the relative distance between the α2 helix of PsaO and Chl a614 of Lhcb2 is shorter in PSI-LHCI-LHCII-ST2 than in maize, which further enhances the contact between PsaO and LHCII on the lumenal side (Supplemental Figure 31). Based on these analyses, we propose that the flatter side of PSI-LHCI-LHCII confers a more stable conformation in higher plants, reducing the rotation of LHCII on the stromal side and improving the EET from LHCII to the PSI core in ST2 (Supplemental Figure 30D).

In summary, our work reveals a model for a further optimized PSI-LHCI structural reorganization in *Arabidopsis*. Upon the transition from ST1 to ST2, the PSI-LHCI supercomplex adopts a more compact configuration, resulting in shorter distances between LHCIs and the PSI core, and conformational changes of PsaA/PsaK/PsaL subsequently facilitate the assembly of PsaO. Moreover, phosphorylation of the LHCII trimer (Lhcb2/Lhcb1/Lhcb1) by the STN7 kinase allows its binding to the docking sites, PsaO/PsaK/PsaL. These two processes together lead to the formation of a PSI-LHCI-LHCII supercomplex and regulate the EET in ST2. This model resolves, to some extent, the long-standing question of whether the phosphorylation of the N terminus of Lhcb2 is sufficient for the binding of the LHCII trimer. The dynamic changes of PsaA/PsaK/PsaL and the stable binding of PsaO are both important for the formation of PSI-LHCI-LHCII-ST2.

METHODS

Plant materials

The A. thaliana Col-0 ecotype and the transfer DNA insertion lines of stn7 (SALK 073254) were used as described previously (Wu et al., 2021). The psan (SALK_088053C) line was obtained from Prof. Y.D. Guo (China Agricultural University). Homozygous transfer DNA insertions of SALK 073254 and SALK_088053C were identified by PCR and sequencing using specific primers (Supplemental Table 10). The psak, psal, psao, and psah1 knockout mutants were generated using the CRISPR-Cas9-based genome editing system, and the targeting sequences (Supplemental Table 10) of these genes were determined and selected based on the offtarget potential of one spacer candidate to other NAG-protospacer adjacent motif (PAM) and NGG-PAM sites (WIMI Biotechnology). Recombinant plasmids of the CRISPR-Cas9 system were transferred into Agrobacterium tumefaciens strain GV3101 and then transformed into the WT background using the floral dipping method. The T1 generation of the transgenic lines was selected on hygromycin-containing Murashige and Skoog medium and grown in a greenhouse to produce seeds for PCR analysis (Supplemental Table 10). After ripening seeds were surface sterilized with 10% sodium hypochlorite and sown on Murashige and Skoog medium supplemented with 3% sucrose. Seedlings were grown under controlled growth chamber conditions as described previously (Wu et al., 2021).

Extraction and purification of the PSI-LHCI-ST1 and PSI-LHCI-LHCII-ST2 supercomplexes

A. thaliana Col-0 ecotype plants were grown under a photon flux density of 80 μ mol of photons m⁻² s⁻¹ with a 12 h light/12 h dark regimen at 22°C. Three-week-old plants were exposed for 90 min to FR light (LED, 730 nm, ST1) and then exposed to white light (ST2) for 90 min. For the native gel samples, thylakoids were solubilized according to a reported protocol (Crepin et al., 2020). The thylakoid membranes were resuspended in 25BTH20G (25 mM BisTris/HCl [pH 7.0], 20% [w/v] glycerol, 10 mM NaF, and 1% protease inhibitor cocktail [4693132001, Roche]) to a Chl concentration of 1.0 mg/ml. Digitonin (D3203, Seaskybio Technology) solution was added to a final concentration of 1.0% and incubated on ice for 10 min. After centrifugation at 8000 rpm at 4°C for 10 min, the soluble membranes (1 μg/μl Chl) were loaded into each lane of PAGE with 50 μl and analyzed by native PAGE. PSI-LHCI-ST1 and PSI-LHCI-LHCII-ST2 supercomplexes were separated by CN-PAGE with a similar method as described previously (Pinnola et al., 2018). After electrophoresis, the target gel bands (about 200 lanes for 1 batch) were cut out and incubated with elution buffer (25 mM BisTris/HCl [pH 7.0], 0.05% digitonin) overnight in a mixer at 4°C. Then the gel mixture was centrifuged at 12 000 rpm at 4°C, and the supernatant was concentrated with a centrifugal filter (Merck Millipore, 30 kDa) and purified using SEC (GE, Superose 6 Increase column 10/300 GL) equilibrated with SEC buffer. The fraction containing the solubilized

supercomplex was concentrated with a centrifugal filter (Merck Millipore, 30 kDa) and used for further analyses.

Characterization of the protein components

The polypeptide composition of thylakoid membranes and purified supercomplexes were analyzed with a sodium dodecyl sulfate (SDS)-PAGE system (Ouyang et al., 2011). Gels were loaded with 1.0 μg Chl and stained with CBB. The purified supercomplexes after SEC were analyzed by high-performance liquid chromatography-MS. Immunoblot analysis was performed using homemade antibodies against PS subunits (PsaA, PsaN, Lhca1, LHCII, Lhcb1, Lhcb2, Lhcb5, D1, and ATPase-β) (Ouyang et al., 2011; Zhang et al., 2021), PsaO (PHY0108A, PhytoAB) and phosphothreonine antibody (9381S, Cell Signaling Technology) with a protein marker (MP102, Vazyme Biotech). The secondary antibody (goat antirabbit immunoglobulin G, OriGene, ZB-2301) conjugated to horseradish peroxidase was used at a dilution of 1/10 000 for detection using the ProLight HRP Chemiluminescent Kit (BE6705, Easybio Technology).

For 2D PAGE, the strips from CN-PAGE were excised and incubated with loading buffer (138 mM Tris/HCl [pH 6.8], 6 M urea, 22.2% [v/v] glycerol, 4.3% w/v] SDS, and 5% [v/v] 2-mercaptoethanol) for 1 h at 25°C. After denaturation, the strips were sealed with 1% agarose, followed by separation of the protein subunits by SDS-PAGE. Gels were stained with CBB or silver (ZD303-1, ZOMANBIO).

Spectral analysis and Chl fluorescence measurements

Samples of thylakoid membranes and purified supercomplexes were diluted with 80% (v/v) acetone for 0.5 h at 4°C. After centrifugation at 12 000 rpm for 10 min, the amounts of Chl a and Chl b of the supernatant were determined using an ultraviolet spectrophotometer (UV/VIS-Lambda 365), and then the Chl a/b ratio was analyzed as described previously (Crepin et al., 2020). The absorption spectra of the original samples from 350-750 nm were measured at room temperature. Fluorescence emission spectroscopy of the original samples at 77 K was recorded (F7000, Hitachi, Japan) by excitation at 435 nm. The emission between 600 and 800 nm was recorded and normalized at 730 nm (Cao et al., 2020). Fluorescence excitation spectroscopy of the original samples at 77 K was performed at 730 nm by excitation from 400-700 nm and normalized at 438 nm (F7000, Hitachi) (Galka et al., 2012; Goss et al., 2017). P700 oxidation and reduction were measured at 705 nm with a Joliot-type spectrophotometer (Bio-Logic SAS JTS-10). The samples were diluted to the same ChI concentration (20 µg/ml ChI) and incubated with an electron donor (3 mM sodium ascorbate) and electron acceptor (1 mM methyl viologen) before starting the measurements.

For intact plants, the ratios of Fv (the variable fluorescence) to Fm (the maxmium fluorescence) and state transition fluorescence were measured with a FluoCam-800MF kinetic imaging fluorimeter (PhotoSystems Instruments) as described previously (Wu et al., 2021). PSI activity was determined with a DualPAM-100 equipped with an ED800T emitter-detector unit as described previously (Zhang et al., 2021) with the following modifications. After a dark adaptation for 20 min, the leaf was illuminated with measuring light and then with FR light (720 nm) to completely oxidize P700. After 30 s, FR light was switched off to rereduce P700 and determine P700_{max}.

Cryo-EM data collection

The PSI–LHCI-ST1 and PSI–LHCI–LHCII-ST2 samples were concentrated to $\sim\!10$ mg protein/ml and applied to the grids within 24 h after purification. Aliquots (3 μ l) of the protein were placed on glow-discharged CryoMatrix R1.2/1.3300-mesh amorphous alloy film (product M024-Au300-R12/13, Zhenjiang Lehua Technology, China) and blotted for 2 s or 3 s under a blot force of 2 or 1 at 100% humidity and 16°C before being flash frozen in liquid ethane with a Mark IV Vitrobot system (Thermo Fisher Scientific). Sample screening was performed using a Talos L120C 120-kV and a Talos F200C 200-kV electron microscope (Thermo Fisher Scientific).

The PSI–LHCI-ST1 video stacks were acquired on a Titan Krios microscope (FEI) operated at 300 kV with a K3 Summit direct electron detector. SerialEM (Mastronarde, 2005) was used for ST1 data at the Institute of Biophysics, Chinese Academy of Sciences. Images were recorded by the beam-image shift data collection methods with a magnification of 22 500× (pixel size 1.07 Å) (Wu et al., 2019). The defocus range was between $-1.2~\mu m$ and $-2.2~\mu m$. Each micrograph was dose fractionated to 32 frames and an exposure time of 8 s, which resulted in a total dose of about 60 $e^-/\mbox{Å}^2$.

PSI-LHCI-LHCII-ST2 video stacks were acquired on a Titan Krios microscope (FEI) operated at 300 kV with a K3 Summit direct electron detector and Quantum energy filter. AutoEMation (Lei and Frank, 2005) was used for automatic data collection at Westlake University. A nominal magnification of 81 000× (pixel size 1.087 Å) was used for imaging. The defocus range was between $-1.2~\mu m$ and $-2.2~\mu m$. Each micrograph was dose fractionated to 32 frames and an exposure time of 2.56 s, which resulted in a total dose of about 50 e $^-/\text{Å}^2$.

Image processing

The data processing flowcharts of PSI-LHCI-ST1 and PSI-LHCI-LHCII-ST2 are shown in Supplemental Figures 5B and 6B. The raw video stacks of the PSI-LHCI-ST1 data were corrected for motion using cryoSPARC 3.2 (Punjani et al., 2017), and contrast transfer function (CTF) parameters of micrographs were estimated using patch-CTF estimation in cryoSPARC (Punjani et al., 2017). Particle picking was performed following methods described previously (Li et al., 2022), resulting in 215 962 particles being selected from 3100 micrographs. To ensure high-quality data, one or two rounds of 2D classification were performed to remove obviously bad or duplicate particles, leaving 155 594 particles for further processing. A subset of particles was used to generate a PSI-LHCI reference and three bad initial models. These particles were subjected to heterogeneous refinement in cryoSPARC, using the previously generated four references. The PSI-LHCI class was selected for further refinement using non-uniform refinement (Punjani et al., 2020), yielding a 3.23-Å map with 95 589 particles. Further refinement was carried out using a round of CTF refinement and non-uniform refinement, ultimately improving the resolution to 3.06 Å. To enhance the quality of the local density of the LHCI region, the signal of the PSI-LHCI region was subtracted, and a mask of the LHCI domain was added for local refinement in cryoSPARC 3.2 (Punjani et al., 2020), leading to an improved local resolution of 3.53 Å.

The same method was applied in the first round of processing for the PSI-LHCI-LHCII-ST2 data, but during the classification process, two separate conformations, PSI-LHCI-ST2 and PSI-LHCI-LHCII-ST2, were identified. For further confirmation, a Topaz (Bepler et al., 2019) particle picking model was retrained. After removing obviously bad particles through 2D classification, heterogeneous refinement was used to classify the remaining 543 767 particles using a PSI-LHCI-LHCII-ST2 reference, a PSI-LHCI-ST2 reference, and four bad references generated by ab initio reconstruction. As a result, an overall resolution of the PSI-LHCI-LHCII map to 2.79 Å was obtained with 188 490 particles, and the PSI-LHCl map was improved to 2.84 Å with 137 602 particles. To further optimize the structure of the LHCI domain of the PSI-LHCI-LHCII-ST2, the densities of PSI and LHCII were subtracted, and a mask was added to the LHCI domain for further optimization of its density through local refinement. The same method was used to optimize the local density of the LHCII domain of PSI-LHCI-LHCII-ST2 and LHCl of the PSI-LHCl-ST2. Finally, the local resolution was improved separately to 3.22 Å, 3.15 Å, and 3.22 Å. To obtain the intact high-resolution density maps for visualization, PHENIX (Liebschner et al., 2019) was used to combine focused density maps and obtain the final overall density maps.

Model building

The cryo-EM map of the PSI-LHCI-LHCII-ST2 supercomplex was obtained at a resolution of 2.79 $\mathring{\rm A}$, allowing the construction of the initial model using

Molecular Plant

State transition-related conformational changes of PSI-LHCI

the PHENIX (Liebschner et al., 2019) automatic software. The atomic models of the ZmPSI-LHCI-LHCII complex (PDB: 5ZJI) (Pan et al., 2018) and the LHCII trimer from the AtPSII (PDB: 5MDX) (Van Bezouwen et al., 2017) were superimposed onto the initial model to assist in building the entire PSI-LHCI-LHCII-ST2 model in Coot (Emsley et al., 2010). High-resolution cryo-EM maps for most of the structures allowed side-chain assignments, with the exception of weak densities in some loops and turns. The entire structure of the PSI-LHCI-LHCII-ST2 supercomplex was further manually adjusted and refined using phenix.real_space_refine, with subsequent iterative rounds of real-space refinement occurring in PHENIX, and the entire structure was further improved through manual adjustments in Coot. The atomic model of the PSI-LHCI-ST1 complex and PSI-LHCI-ST2 were built using the structure of the PSI-LHCI-LHCII-ST2 supercomplex as a starting model, with the initial model manually adjusted and fitted into the cryo-EM map in UCSF ChimeraX (Pettersen et al., 2021), followed by several cycles of model building in Coot and real-space refinement using PHENIX performed manually. All complex structures were refined using PHENIX with phenix.real_space_refine. The statistics of the refinements are listed in Table S4. Structural figures were prepared using the PyMOL (www.pymol. org), Chimera (Pettersen et al., 2004), and ChimeraX software packages.

Statistical analysis

Statistical parameters are reported in the figures and corresponding figure legends. Data of ChI concentrations and PSI activity were expressed as mean \pm SEM. All experiments related to seedlings and imaging studies were performed in a blinded fashion. None of the data were removed from our statistical analysis as outliers. The obtained relative intensities and values were plotted in Origin 2022 software.

DATA AVAILABILITY

Cryo-EM maps and coordinates have been deposited in the EMDB and wwPDB, respectively: PSI-LHCI-ST1 (composite cryo-EM map, EMD-36036; consensus refinement map, EMD-36033; PDB: 8J7A), PSI-LHCI-ST2 (composite cryo-EM map, EMD-36037; consensus refinement map, EMD-36026; PDB: 8J7B), PSI-LHCI-LHCII-ST2 (composite cryo-EM map, EMD-36021; consensus refinement map, EMD-36020; PDB: 8J6Z), LHCI of PSI-LHCI-ST1 (focused refinement map, EMD-36035), LHCI of PSI-LHCI-ST2 (focused refinement map, EMD-36032), LHCI of PSI-LHCI-LHCII-ST2 (focused refinement map, EMD-36022), and LHCII of PSI-LHCI-LHCII-ST2 (focused refinement map, EMD-36023).

SUPPLEMENTAL INFORMATION

Supplemental information is available at Molecular Plant Online.

FUNDING

This work was supported by the National Key Research and Development Program of China (2020YFA0907600 to L.Z.) and the National Natural Science Foundation of China (National Science Foundation of China) (32241030 to S.S.).

AUTHOR CONTRIBUTIONS

J.W. performed extraction and purification of the supercomplexes, cryo-EM sample preparation and data collection, and genetic and physiological experiments. S.C. performed cryo-EM data image processing and reconstruction and results analysis. C.W. performed cryo-EM data collection and reconstruction. W.L. assisted with protein purification, sample preparation, and cryo-EM data collection. C.H. and C.F. assisted with protein purification and genetic experiments. J.W, S.C., S.S., and L.Z. conceived the project, analyzed the data, and wrote the paper. All authors discussed the results and commented on the manuscript.

ACKNOWLEDGMENTS

We would like to thank the Center for Biological Imaging (CBI), Institute of Biophysics (IBP), Chinese Academy of Science (CAS) for our cryo-EM work, and we are grateful to Boling Zhu, Xujing Li, Binxuan Huangfu, Longlong Zhang, Xiaojun Huang, and Fei Sun for help with preparing EM samples and taking EM images. We thank the cryo-EM facility of Westlake University for help with data collection (PSI-LHCI-LHCII-ST2); Dr. Jun He from the Guangzhou Institutes of Biomedicine and Health (GIBH), Chinese Academy of Sciences, for help with screening cryo-EM samples; Xiaoyun Wang and Prof. Yangdong Guo from China Agricultural University for providing the Arabidopsis mutants; Fang Sun from IBP, CAS, for zealous help with the cryo-EM sample preparation for Vitrobot; Chunyan Zhang from the Institute of Botany, CAS, for technical support with the measurement of P700 activity; and Xiahe Huang and Yingchun Wang from the Institute of Genetics and Developmental Biology, CAS, for technical support with mass spectrometry. We sincerely appreciate Prof. Xiaoling Xu and Dr. Jiyu Xin from Hangzhou Normal University for help with the data analysis of cryo-EM and manuscript preparation. We are grateful to Dr. Yanan Xiao, Prof. Jean-David Rochaix, and Jianren Shen for revising the manuscript. No conflict of interest is declared.

Received: June 10, 2023 Revised: September 12, 2023 Accepted: November 6, 2023 Published: November 7, 2023

REFERENCES

Amunts, A., Drory, O., and Nelson, N. (2007). The structure of a plant photosystem I supercomplex at 3.4 Å resolution. Nature 447:58–63.

Bellafiore, S., Barneche, F., Peltier, G., and Rochaix, J.D. (2005). State transitions and light adaptation require chloroplast thylakoid protein kinase STN7. Nature 433:892–895.

Ben-Shem, A., Frolow, F., and Nelson, N. (2003). Crystal structure of plant photosystem I. Nature **426**:630–635.

Bepler, T., Morin, A., Rapp, M., Brasch, J., Shapiro, L., Noble, A.J., and Berger, B. (2019). Positive-unlabeled convolutional neural networks for particle picking in cryo-electron micrographs. Nat. Methods. 16:1153–1160.

Caffarri, S., Kouril, R., Kereïche, S., Boekema, E.J., and Croce, R. (2009). Functional architecture of higher plant photosystem II supercomplexes. EMBO J. 28:3052–3063.

Cao, P., Cao, D., Si, L., Su, X., Tian, L., Chang, W., Liu, Z., Zhang, X., and Li, M. (2020). Structural basis for energy and electron transfer of the photosystem I-IsiA-flavodoxin supercomplex. Nat. Plants 6:167–176.

Caspy, I., Malavath, T., Klaiman, D., Fadeeva, M., Shkolnisky, Y., and Nelson, N. (2020). Structure and energy transfer pathways of the Dunaliella Salina photosystem I supercomplex. Biochim. Biophys. Acta. Bioenerg. 1861:148253.

Caspy, I., Neumann, E., Fadeeva, M., Liveanu, V., Savitsky, A., Frank, A., Kalisman, Y.L., Shkolnisky, Y., Murik, O., Treves, H., et al. (2021). Cryo-EM photosystem I structure reveals adaptation mechanisms to extreme high light in *Chlorella ohadii*. Nat. Plants **7**:1314–1322.

Crepin, A., and Caffarri, S. (2015). The specific localizations of phosphorylated Lhcb1 and Lhcb2 isoforms reveal the role of Lhcb2 in the formation of the PSI-LHCII supercomplex in *Arabidopsis* during state transitions. Biochim. Biophys. Acta **1847**:1539–1548.

Crepin, A., Kučerová, Z., Kosta, A., Durand, E., and Caffarri, S. (2020). S. Isolation and characterization of a large photosystem I-light-harvesting complex II supercomplex with an additional Lhca1-a4 dimer in *Arabidopsis*. Plant J. 102:398–409.

Croce, R., and Van Amerongen, H. (2020). Light harvesting in oxygenic photosynthesis: structural biology meets spectroscopy. Science 369:eaay2058.

- Depège, N., Bellafiore, S., and Rochaix, J.D. (2003). Role of chloroplast protein kinase Stt7 in LHCII phosphorylation and state transition in *Chlamydomonas*. Science **299**:1572–1575.
- Drop, B., Webber-Birungi, M., Yadav, S.K.N., Filipowicz-Szymanska, A., Fusetti, F., Boekema, E.J., and Croce, R. (2014). Light-harvesting complex II (LHCII) and its supramolecular organization in *Chlamydomonas reinhardtii*. Biochim. Biophys. Acta **1837**:63–72.
- Eberhard, S., Finazzi, G., and Wollman, F.A. (2008). The dynamics of photosynthesis. Annu. Rev. Genet. 42:463–515.
- Elrad, D., Niyogi, K.K., and Grossman, A.R. (2002). A major light-harvesting polypeptide of photosystem II functions in thermal dissipation. Plant Cell 14:1801–1816.
- Emsley, P., Lohkamp, B., Scott, W.G., and Cowtan, K. (2010). Features and development of Coot. Acta Crystallogr. D Biol. Crystallogr. 66:486–501.
- Ferrante, P., Ballottari, M., Bonente, G., Giuliano, G., and Bassi, R. (2012). LHCBM1 and LHCBM2/7 polypeptides, components of major LHCII complex, have distinct functional roles in photosynthetic antenna system of *Chlamydomonas reinhardtii*. J. Biol. Chem. **287**:16276–16288.
- Galka, P., Santabarbara, S., Khuong, T.T.H., Degand, H., Morsomme, P., Jennings, R.C., Boekema, E.J., and Caffarri, S. (2012). Functional analyses of the plant photosystem I-light-harvesting complex II supercomplex reveal that light-harvesting complex II loosely bound to photosystem II is a very efficient antenna for photosystem I in state II. Plant Cell 24:2963–2978.
- Goss, R., Greifenhagen, A., Bergner, J., Volke, D., Hoffmann, R., Wilhelm, C., and Schaller-Laudel, S. (2017). Direct isolation of a functional violaxanthin cycle domain from thylakoid membranes of higher plants. Planta 245:793–806.
- Govindjee, S.D., Shevela, D., and Björn, L.O. (2017). Evolution of the Z-scheme of photosynthesis: a perspective. Photosynth. Res. 133:5–15.
- Huang, Z., Shen, L., Wang, W., Mao, Z., Yi, X., Kuang, T., Shen, J.R., Zhang, X., and Han, G. (2021). Structure of photosystem I-LHCI-LHCII from the green alga *Chlamydomonas reinhardtii* in state 2. Nat. Commun. 12:1100.
- Jensen, P.E., Gilpin, M., Knoetzel, J., and Scheller, H.V. (2000). The PSI-K subunit of photosystem I is involved in the interaction between light-harvesting complex I and the photosystem I reaction center core. J. Biol. Chem. 275:24701–24708.
- Jensen, P.E., Haldrup, A., Zhang, S., and Scheller, H.V. (2004). The PSI-O subunit of plant photosystem I is involved in balancing the excitation pressure between the two photosystems. J. Biol. Chem. 279:24212– 24217.
- Koskela, M.M., Brünje, A., Ivanauskaite, A., Grabsztunowicz, M., Lassowskat, I., Neumann, U., Dinh, T.V., Sindlinger, J., Schwarzer, D., Wirtz, M., et al. (2018). Chloroplast acetyltransferase NSI is required for state transitions in *Arabidopsis thaliana*. Plant Cell 30:1695–1709.
- Koskela, M.M., Brünje, A., Ivanauskaite, A., Lopez, L.S., Schneider, D., DeTar, R.A., Kunz, H.H., Finkemeier, I., and Mulo, P. (2020). Comparative analysis of thylakoid protein complexes in state transition mutants *nsi* and *stn7*: focus on PSI and LHCII. Photosynth. Res. 145:15–30.
- Lei, J., and Frank, J. (2005). Automated acquisition of cryo-electron micrographs for single particle reconstruction on an FEI Tecnai electron microscope. J. Struct. Biol. 150:69–80.
- Lemeille, S., and Rochaix, J.D. (2010). State transitions at the crossroad of thylakoid signalling pathways. Photosynth. Res. **106**:33–46.
- Leoni, C., Pietrzykowska, M., Kiss, A.Z., Suorsa, M., Ceci, L.R., Aro, E.M., and Jansson, S. (2013). Very rapid phosphorylation kinetics

- suggest a unique role for Lhcb2 during state transitions in *Arabidopsis*. Plant J. **76**:236–246.
- Li, Z., Chen, S., Zhao, L., Huang, G., Pi, X., Sun, S., Wang, P., and Sui, S.F. (2022). Near-atomic structure of the inner ring of the Saccharomyces cerevisiae nuclear pore complex. Cell Res. 32:437–450.
- Liebschner, D., Afonine, P.V., Baker, M.L., Bunkóczi, G., Chen, V.B., Croll, T.I., Hintze, B., Hung, L.W., Jain, S., McCoy, A.J., et al. (2019). Macromolecular structure determination using X-rays, neutrons and electrons: recent developments in Phenix. Acta. Crystallogr. D. Struct. Biol. **75**:861–877.
- Longoni, P., Douchi, D., Cariti, F., Fucile, G., and Goldschmidt-Clermont, M. (2015). Phosphorylation of the light-harvesting complex II isoform Lhcb2 is central to state transitions. Plant Physiol. 169:2874–2883.
- **Mastronarde, D.N.** (2005). Automated electron microscope tomography using robust prediction of specimen movements. J. Struct. Biol. **152**:36–51.
- Mazor, Y., Nataf, D., Toporik, H., and Nelson, N. (2013). Crystal structures of virus-like photosystem I complexes from the mesophilic cyanobacterium *Synechocystis PCC 6803*. Elife **3**, e01496.
- Mazor, Y., Borovikova, A., and Nelson, N. (2015). The structure of plant photosystem I super-complex at 2.8 Å resolution. Elife 4, e07433.
- Mazor, Y., Borovikova, A., Caspy, I., and Nelson, N. (2017). Structure of the plant photosystem I supercomplex at 2.6 Å resolution. Nat. Plants 3. 17014.
- Naschberger, A., Mosebach, L., Tobiasson, V., Kuhlgert, S., Scholz, M., Perez-Boerema, A., Ho, T.T.H., Vidal-Meireles, A., Takahashi, Y., Hippler, M., et al. (2022). Algal photosystem I dimer and high-resolution model of PSI-plastocyanin complex. Nat. Plants 8:1191–1201.
- **Nelson, N., and Yocum, C.F.** (2006). Structure and function of photosystems I and II. Annu. Rev. Plant Biol. **57**:521–565.
- Ouyang, M., Li, X., Ma, J., Chi, W., Xiao, J., Zou, M., Chen, F., Lu, C., and Zhang, L. (2011). LTD is a protein required for sorting light-harvesting chlorophyll-binding proteins to the chloroplast SRP pathway. Nat. Commun. 2:277.
- Ouyang, M., Li, X., Zhang, J., Feng, P., Pu, H., Kong, L., Bai, Z., Rong, L., Xu, X., Chi, W., et al. (2020). Liquid-liquid phase transition drives intra-chloroplast cargo sorting. Cell 180:1144–1159.e20.
- Pan, X., Ma, J., Su, X., Cao, P., Chang, W., Liu, Z., Zhang, X., and Li, M. (2018). Structure of the maize photosystem I supercomplex with light-harvesting complexes I and II. Science 360:1109–1113.
- Pan, X., Cao, P., Su, X., Liu, Z., and Li, M. (2020). Structural analysis and comparison of light-harvesting complexes I and II. Biochim. Biophys. Acta Bioenerg. 1861, 148038.
- Pan, X., Tokutsu, R., Li, A., Takizawa, K., Song, C., Murata, K., Yamasaki, T., Liu, Z., Minagawa, J., and Li, M. (2021). Structural basis of LhcbM5-mediated state transitions in green algae. Nat. Plants 7:1119–1131.
- Pettersen, E.F., Goddard, T.D., Huang, C.C., Couch, G.S., Greenblatt, D.M., Meng, E.C., and Ferrin, T.E. (2004). UCSF Chimera-a visualization system for exploratory research and analysis. J. Comput. Chem. 25:1605–1612.
- Pettersen, E.F., Goddard, T.D., Huang, C.C., Meng, E.C., Couch, G.S., Croll, T.I., Morris, J.H., and Ferrin, T.E. (2021). UCSF ChimeraX: Structure visualization for researchers, educators, and developers. Protein Sci. 30:70–82.
- Pi, X., Tian, L., Dai, H.E., Qin, X., Cheng, L., Kuang, T., Sui, S.F., and Shen, J.R. (2018). Unique organization of photosystem I-light-

- harvesting supercomplex revealed by cryo-EM from a red alga. Proc. Natl. Acad. Sci. USA 115:4423-4428.
- Pietrzykowska, M., Suorsa, M., Semchonok, D.A., Tikkanen, M., Boekema, E.J., Aro, E.M., and Jansson, S. (2014). The lightharvesting chlorophyll a/b binding proteins Lhcb1 and Lhcb2 play complementary roles during state transitions in Arabidopsis. Plant Cell 26:3646-3660.
- Pinnola, A., Alboresi, A., Nosek, L., Semchonok, D., Rameez, A., Trotta, A., Barozzi, F., Kouřil, R., Dall'Osto, L., Aro, E.M., et al. (2018). A LHCB9-dependent photosystem I megacomplex induced under low light in Physcomitrella patens. Nat. Plants 4:910-919.
- Punjani, A., Rubinstein, J.L., Fleet, D.J., and Brubaker, M.A. (2017). cryoSPARC: algorithms for rapid unsupervised cryo-EM structure determination. Nat. Methods 14:290-296.
- Pribil, M., Pesaresi, P., Hertle, A., Barbato, R., and Leister, D. (2010). Role of plastid protein phosphatase TAP38 in LHCII dephosphorylation and thylakoid electron flow. PLoS Biol. 8, e1000288.
- Qin, X., Suga, M., Kuang, T., and Shen, J.R. (2015). Structural basis for energy transfer pathways in the plant PSI-LHCI supercomplex. Science 348:989-995.
- Punjani, A., Zhang, H., and Fleet, D.J. (2020). Non-uniform refinement: adaptive regularization improves single-particle cryo-EM reconstruction. Nat. Methods. 17:1214-1221.
- Qin, X., Pi, X., Wang, W., Han, G., Zhu, L., Liu, M., Cheng, L., Shen, J.R., Kuang, T., and Sui, S.F. (2019). Structure of a green algal photosystem I in complex with a large number of light-harvesting complex I subunits. Nat. Plants 5:263-272.
- Rochaix, J.D. (2013). Redox regulation of thylakoid protein kinases and photosynthetic gene expression. Antioxidants Redox Signal. **18**:2184–2201.
- Rochaix, J.D. (2014). Regulation and dynamics of the light-harvesting system. Annu. Rev. Plant Biol. 65:287-309.
- Shapiguzov, A., Ingelsson, B., Samol, I., Andres, C., Kessler, F., Rochaix, J.D., Vener, A.V., and Goldschmidt-Clermont, M. (2010). The PPH1 phosphatase is specifically involved in LHCII dephosphorylation and state transitions in Arabidopsis. Proc. Natl. Acad. Sci. USA 107:4782-4787.
- Shapiguzov, A., Chai, X., Fucile, G., Longoni, P., Zhang, L., and Rochaix, J.D. (2016). Activation of the Stt7/STN7 kinase through dynamic interactions with the cytochrome $b_6 f$ complex. Plant Physiol. 171:82-92.

- Suga, M., Ozawa, S.I., Yoshida-Motomura, K., Akita, F., Miyazaki, N., and Takahashi, Y. (2019). Structure of the green algal photosystem I supercomplex with a decameric light-harvesting complex I. Nat. Plants 5:626-636.
- Su, X., Ma, J., Wei, X., Cao, P., Zhu, D., Chang, W., Liu, Z., Zhang, X., and Li, M. (2017). Structure and assembly mechanism of plant C2S2M2-type PSII-LHCII supercomplex. Science 357:815-820.
- Su, X., Ma, J., Pan, X., Zhao, X., Chang, W., Liu, Z., Zhang, X., and Li, M. (2019). Antenna arrangement and energy transfer pathways of a green algal photosystem-I-LHCI supercomplex. Nat. Plants 5:273-281.
- Tikkanen, M., Piippo, M., Suorsa, M., Sirpiö, S., Mulo, P., Vainonen, J., Vener, A.V., Allahverdiyeva, Y., and Aro, E.M. (2006). State transitions revisited-a buffering system for dynamic low light acclimation of Arabidopsis. Plant Mol. Biol. 62:779-793.
- Van Bezouwen, L.S., Caffarri, S., Kale, R.S., Kouřil, R., Thunnissen, A.M.W.H., Oostergetel, G.T., and Boekema, E.J. (2017). Subunit and chlorophyll organization of the plant photosystem II supercomplex. Nat. Plants 3, 17080.
- Varotto, C., Pesaresi, P., Jahns, P., Lessnick, A., Tizzano, M., Schiavon, F., Salamini, F., and Leister, D. (2002). Single and double knockouts of the genes for photosystem I subunits G, K, and H of Arabidopsis. Effects on photosystem I composition, photosynthetic electron flow, and state transitions. Plant Physiol. **129**:616-624.
- Wang, J., Yu, L.-J., Wang, W., Yan, Q., Kuang, T., Qin, X., and Shen, J.-R. (2021). Structure of plant photosystem I-light harvesting complex I supercomplex at 2.4 Å resolution. J. Integr. Plant Biol. 7:1367–1381.
- Wu, J., Rong, L., Lin, W., Kong, L., Wei, D., Zhang, L., Rochaix, J.D., and Xu, X. (2021). Functional redox links between lumen thiol oxidoreductase1 and serine/threonine-protein kinase STN7. Plant Physiol. **186**:964–976.
- Wu, C., Huang, X., Cheng, J., Zhu, D., and Zhang, X. (2019). Highquality, high-throughput cryo-electron microscopy data collection via beam tilt and astigmatism-free beam-image shift. J. Struct. Biol. 208, 107396.
- Zhang, J., Bai, Z., Ouyang, M., Xu, X., Xiong, H., Wang, Q., Grimm, B., Rochaix, J.D., and Zhang, L. (2021). The DnaJ proteins DJA6 and DJA5 are essential for chloroplast iron-sulfur cluster biogenesis. EMBO J. 40, e106742.
- Zhang, S., Tang, K., Yan, Q., Li, X., Shen, L., Wang, W., He, Y.K., Kuang, T., Han, G., Shen, J.R., et al. (2023). Structural insights into a unique PSI-LHCI-LHCII-Lhcb9 supercomplex from moss Physcomitrium patens. Nat. Plants 9:832-846.